Microstructural analysis of slag properties associated with calcite precipitation due to passive CO_2 mineralization

Faisal W.K. Khudhur [a,*], John M. MacDonald [a], Luke Daly [a,b,c], Alice Macente [a,d,e], Liene Spruženiece [a,f], Sammy Griffin [a], Claire Wilson [g]

[a] School of Geographical and Earth Sciences, University of Glasgow, Glasgow G12 8QQ, UK
[b] Australian Centre for Microscopy and Microanalysis, University of Sydney, Sydney 2006, NSW, Australia
[c] Department of Materials, University of Oxford, Oxford OX1 3PH, UK
[d] Department of Civil and Environmental Engineering, University of Strathclyde, Glasgow G1 1XJ, UK
[e] School of Civil Engineering, University of Leeds, Leeds LS2 9JT, UK
[f] Geoanalytical Electron Microscopy and Spectroscopy (GEMS) Laboratory, University of Glasgow, Glasgow G12 8QQ, UK
[g] School of Chemistry, University of Glasgow, Glasgow G12 8QQ, UK

ARTICLE INFO

ABSTRACT

CO_2 mineralization in slag has gained significant attention since it occurs with minimal human intervention and energy input. While the amount of theoretical CO_2 that can be captured within slag has been quantified based on slag composition in several studies, the microstructural and mineralogical effects of slag on its ability to capture CO_2 have not been fully addressed. In this work, the CO_2 uptake within legacy slag samples is analyzed through microstructural characterization. Slag samples were collected from the former Ravenscraig steelmaking site in Lanarkshire, Scotland. The collected samples were studied using X-ray Computed Tomography (XCT) to understand the distribution and geometry of pore space, as well as with scanning electron microscopy (SEM) coupled with energy-dispersive X-ray spectroscopy (EDS) to visualize the distribution of elements within the studied samples. Electron backscatter diffraction (EBSD) was used to study the minerals distribution. The samples were also characterized through X-ray diffraction (XRD) and X-ray fluorescence (XRF), and the amount of captured CO_2 was quantified using thermogravimetric analysis (TGA). Our results demonstrate that CO_2 uptake occurs to the extent of ~9–30 g CO_2/ kg slag. The studied samples are porous in nature, with pore space occupying up to ~30% of their volumes, and they are dominated by åkermanite-gehlenite minerals which interact with the atmospheric CO_2 slowly at ambient conditions. EDS and EBSD results illustrate that the precipitated carbonate in slag is calcite, and that the precipitation of calcite is accompanied by the formation of a Si-O-rich layer. The provided analysis concludes that the porous microstructure as well as the minerals distribution in slag should be considered in forecasting and designing large-scale solutions for passive CO_2 mineralization in slag.

1. Introduction

Ironmaking and steelmaking industries emit ~400 kg CO_2 / 1000 kg of pig iron and produce 200 kg slag / 1000 kg of steel, making CO_2 emission and slag among the biggest challenges faced by these industries (Gomes et al., 2016; World Steel Association, 2017). Slag is produced as a by-product during the refining of iron and steel, and it is mainly composed of calcium, magnesium and iron silicates. It can contain several mineral phases such as åkermanite ($Ca_2MgSi_2O_7$), gehlenite ($Ca_2Al_2SiO_7$), larnite (Ca_2SiO_4) and portlandite ($Ca(OH)_2$), and its

properties such as chemical and mineralogical compositions, crystallinity and size distribution depend on its production pathway and disposal methods (Chukwuma et al., 2021). CO_2 mineralization in slag has been widely investigated as a potential CO_2 capture and sequestration (CCS) process (Khudhur et al., 2022a; Mayes et al., 2018; Pullin et al., 2019; Renforth et al., 2011; Riley et al., 2020) and the references therein). This process is based on reactions in which slag minerals such as larnite and gehlenite weather and dissolve to produce SiO_2 and to provide Ca cations. These cations react with atmospheric CO_2, which forms carbonic acid (H_2CO_3) upon dissolution in water, to precipitate

calcite ($CaCO_3$), as summarized in the following equations (Béarat et al., 2006; Lackner et al., 1995; Pullin et al., 2019):

$$Ca_2SiO_4 + 2H_2CO_3 \rightarrow 2CaCO_3 + 2H_2O + SiO_2 \tag{1}$$

$$2Ca_2Al_2SiO_7 + 2H_2CO_3 \rightarrow 2CaCO_3 + 2H_2O + Al_2O_3 + SiO_2 \tag{2}$$
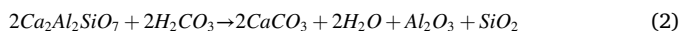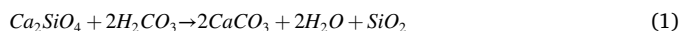
The suitability of slag for CO_2 mineralization is attributed to its chemical composition, as predicted through Steinor's equation (Huntzinger et al., 2009; Renforth, 2019):

$$C_{pot} = \frac{MW_{CO_2}}{100}\left(\alpha\frac{CaO}{MW_{CaO}} + \beta\frac{MgO}{MW_{MgO}} + \gamma\frac{SO_3}{MW_{SO_3}} + \delta\frac{P_2O_5}{MW_{P_2O_5}}\right) \times 1000 \tag{3}$$

Where C_{pot} refers to the carbonation potential (kg CO_2 uptake/1000 kg wastes) and MW_X refers to the molar of component X. CaO, MgO, SO_3 and P_2O_5 refer to the percentages of the corresponding compounds, and the coefficients (α, β, γ, δ) reflect the contribution of each compound, respectively. Basic oxides (such as calcium and magnesium oxides) and acidic oxides (such as sulfur and phosphorus oxides) result in high and low CO_2 uptake potential, respectively (Gunning et al., 2010; Renforth, 2019). The produced calcite is thermodynamically stable over geologic timescale, with a thermal decomposition temperature above 500 °C (Huijgen et al., 2005). Therefore, many studies have examined how calcite precipitation can be optimized as a method of CO_2 uptake (Khudhur et al., 2022b; Renforth et al., 2015).

Recently, there has been increased emphasis on relating materials' microstructural properties to their CO_2 uptake potential as reactions may proceed at rates that are scale-dependents (Zachara et al., 2016). Scanning Electron Microscopy (SEM) coupled with Energy Dispersive Spectroscopy (EDS) has been used to study the CO_2 mineralization reaction at the micro-nanoscale to determine factors that limit CO_2 uptake in different materials. For example, Sun et al. (2019) used SEM-EDS analysis to study the CO_2 uptake in CaO particles at elevated temperature (600 °C) and demonstrated that as the reaction progressed, a 90-nm thick layer of calcium carbonates ($CaCO_3$) formed around CaO particles. This layer created a barrier that hindered the carbonation reaction, by preventing CO_2 from reaching reactive sites on CaO particles. Electron backscatter diffraction (EBSD) is another SEM-based technique that has been employed to study the microstructural features of a given sample such as texture, crystallographic orientation and grain boundaries. Such information enhances understanding of the carbonation process as materials properties such as dissolution, precipitation and reactivity may be anisotropic (Mariano et al., 2017; Peuble et al., 2015). For example, Mayorga et al. (2018) demonstrated that the highest density of calcite precipitation and growth occurred on the (100) face of anhydrite ($CaSO_4$), suggesting that calcite precipitation on a given substrate could be enhanced if the latter was manufactured to produce crystals at a given orientation. Another technique that is used in studying mineral carbonation is X-ray Computed Tomography (XCT). This technique yields a 3D microstructural reconstruction of a given sample, which can be used to analyze pore space and flow properties in materials of interest, thereby linking carbonates precipitation to transport properties. Boone et al. (2014) used XCT to study the carbonation of pulverized slag and demonstrated that calcite precipitation occurred in pores having a maximum equivalent diameter of 50 μm. Field-based studies documented passive CO_2 uptake in legacy slag heaps and demonstrated that atmospheric CO_2 can be sequestered in slag with minimal human intervention (Khudhur et al., 2022b; MacDonald et al., 2023). However, Pullin et al. (2019) noted that the observed CO_2 uptake was as low as ~3% of the total CO_2 uptake potential of slag heaps, where the maximum CO_2 uptake potential is calculated based on the slag content of metal oxides. Such low CO_2 uptake was attributed to waste management practices that reduce the interaction of CO_2 with slag and to the low watering frequency that resulted in low leaching of calcium ions and low supply of carbonates, consequently low carbonates precipitation.

Despite the increased awareness of the possibility of using slag in carbon capture applications, limited research has been conducted regarding the microstructure of slag and its effect on CO_2 uptake. In this work, we document CO_2 uptake through passive mineralization that has occurred in slag at the former Ravenscraig steel worksite in Scotland for more than 30 years. Additionally, we report several properties of slag that affect this CO_2 uptake process. In addition to performing the thermogravimetric analysis (TGA), X-ray diffraction (XRD) and X-ray fluorescence (XRF), we characterize the slag microstructure using XCT to reveal the 3D pore space and to visualize the reactive surface area. This is followed by analyzing the elements distribution and mineralogical properties in the studied samples using EDS and EBSD analyses, respectively. Results from these analyses are used to understand calcite precipitation patterns in slag and to give insights into what factors dictate CO_2 uptake in this material. We used relevant literature to relate the observed properties to the CO_2 uptake in the studied materials and highlight that in addition to the chemical composition, other microstructural and mineralogical properties should be evaluated for accurate forecast of passive CO_2 mineralization when deployed on a large scale.

2. Materials and methods

Four samples were collected from the former Ravenscraig steelworks in Motherwell, Scotland (55°47′21″ N, 3°56′25″ W), as shown in supplementary Fig. S1. At the studied site, annual temperatures range from 8.0° to 9.4°C, while the annual rainfall is less than 1000 mm (Met Office, 2016). By hosting one of the largest continuous casting, rolling mills, blast furnaces and basic oxygen steel production facilities in the world, Ravenscraig was considered to be the steel production capital in Scotland and one of the biggest steel producers in the United Kingdom (Ioris, 2014; Stewart, 2008). In 1992, however, steelworks operations were terminated, and the demolition of steel plants took place in 1996, creating the largest brownfield in Europe. Since then, efforts have been made to enhance and develop the area, although there are concerns related to pollution as brownfields and slag heaps can be sources of different pollutants (Gomes et al., 2018; Land Use Consultant, 2008). The collected slag samples (samples A through D) were cut into small cuboids with an edge length of ~1 cm using a water-cooled diamond saw for analysis. The samples were immediately dried with paper towels and placed in a heated oven (<60 °C) under reduced pressure and subsequently placed in plastic bags to minimize their interaction with the atmosphere.

X-ray Computed Tomography was used to visualize the internal microstructure of the samples, including the volume fractions of phases, porosity, pore connectivity and reactive surface area. The prepared samples were imaged using a Nikon XT H320 LC X-ray Computed Tomography system in the Civil and Environmental Engineering department at the University of Strathclyde. For each sample, the acquired 2D images were stacked to produce a 3D volume that contains the attenuation information. This volume was used to visualize the internal microstructure of the studied sample and to identify regions of interest for further analysis. After identifying those regions, a water-cooled saw was used to cut the sample to expose them so they can be further analyzed with SEM-based techniques. XCT equipment settings are summarized in supplementary Table S1.

SEM-EDS-EBSD analyses were used to obtain elements and minerals distributions as well as crystallographic features of the samples. Once areas of interest were identified and exposed, the samples were embedded in resin (Buehler, USA), polished and carbon coated. Backscatter electrons (BSE) and EDS signal were collected using Zeiss Sigma VP Field-Emission Gun SEM (VP-FEG-SEM) equipped with an X-Max 80 mm^2 silicon drift EDS detector based in the GEMS facility at the University of Glasgow. For EBSD analysis, the samples were polished using silicon carbide papers, down to P4000 (<5 μm) level. This was followed by polishing them using 3 μm, 1 μm, 0.35 μm oil-based diamond suspensions followed by colloidal silica. EBSD patterns were
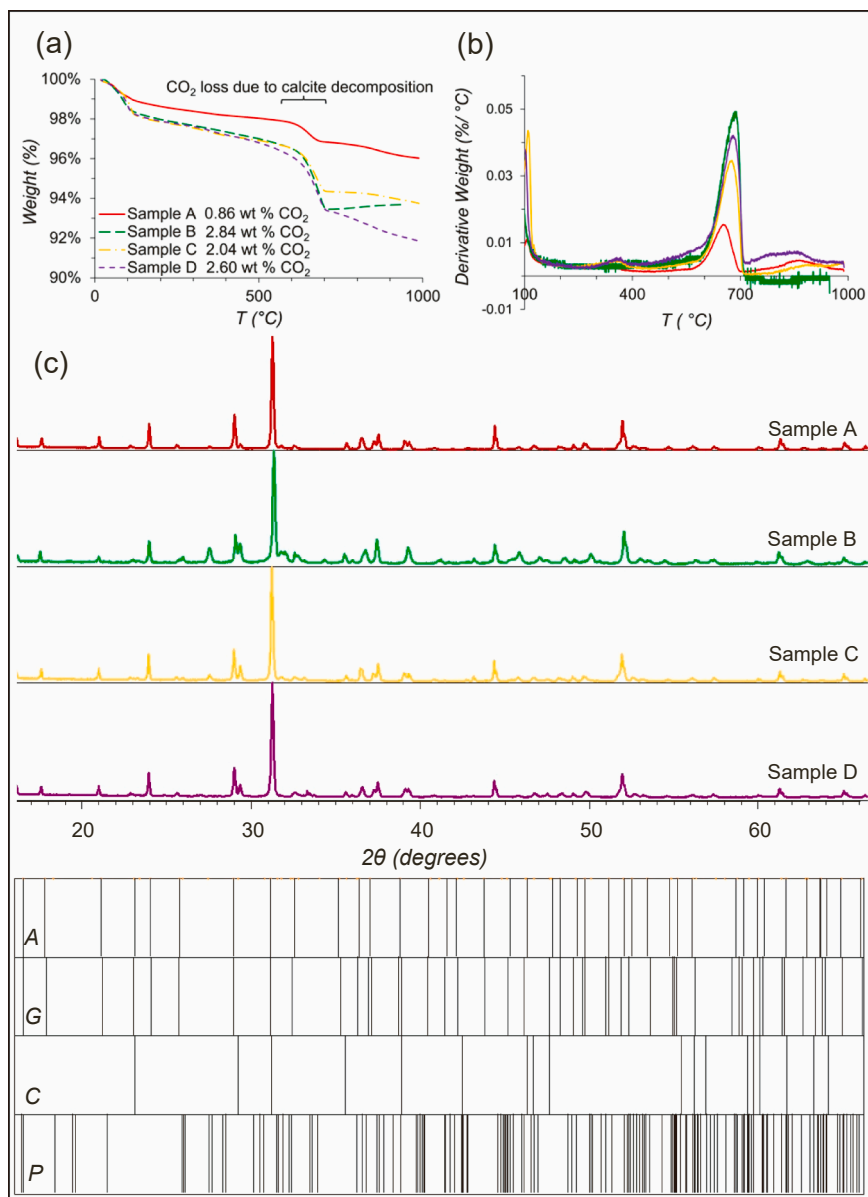
Fig. 1. (a) TGA thermograms of the samples, also showing CO$_2$ content. (b) Derivative thermogravimetric curve (DTG). (c) XRD results, showing the studied samples' diffractograms and the peaks locations for standard åkermanite (A), gehlenite (G), calcite (C) and pseudowollastonite (P).

collected using Symmetry S2 EBSD detector (Oxford Instrument). BSE images, EDS signals and EBSD patterns were acquired across regions of interest and were analyzed with Oxford Instrument AZTec ® 6.0 and Aztec Crystal ® 2.2 software. EBSD patterns were indexed using Inorganic Crystal Structure Database (ICSD) and HKL phases (Zagorac et al., 2019). Equipment settings are summarized in supplementary Table S1, while EBSD analysis parameters were adapted from Griffin et al. (2023) and are summarized in supplementary Table S2. EDS/EBSD results were used to guide the XCT segmentation process as explained in supplementary note 3.

The samples XCT images were segmented into four phases using the trainable WEKA segmentation 2D plugin (TWS) in the Fiji distribution of ImageJ (Schindelin et al., 2012). The four phases are the pore space, calcite, åkermanite-gehlenite dominated matrix, and the last miscellaneous phase that included anything else that did not fall under the previous categories, such as silica and other precipitates in pores. Segmentation results were visualized using Avizo ® 9.3.0 software, and they were post-processed by removing islands smaller than 3×3x3 voxels. Details of image processing workflow, including phase quantification

modules and error calculations are documented in our previous work where sample B was used in designing the image processing workflow that is used in this work (Khudhur et al., 2022b). XCT, BSE, EDS, TGA and XRD data acquired on Sample B in our previous study are also included here to provide coherent understanding regarding CO$_2$ mineralization in slag and to facilitate comparison. In this work, we provided more in-depth analysis about the pore space by studying equivalent diameters and connectivity using OpenPNM tool available within DragonFly ® software (Gostick et al., 2016). Details of the image analysis are summarized in the supplementary note 3 and in supplementary Figs. S2 and S3.

XRD, TGA and XRF analyses were used to study the bulk properties of the samples, namely the present minerals, the CO$_2$ content and the composition of the studied samples, respectively. Offcuts from the samples were pulverized using pestle and mortar and sieved. Particles smaller than 53 μm were retained for analysis. XRD analysis was performed using PANalytical X'Pert Pro diffractometer (Malvern Panalytical) equipped with Cu Kα1 (λ = 1.5406 Å) X-radiation from a Cu target sealed tube with monochromator in reflection geometry with

Table 1
Bulk chemical compositions through XRF analysis.

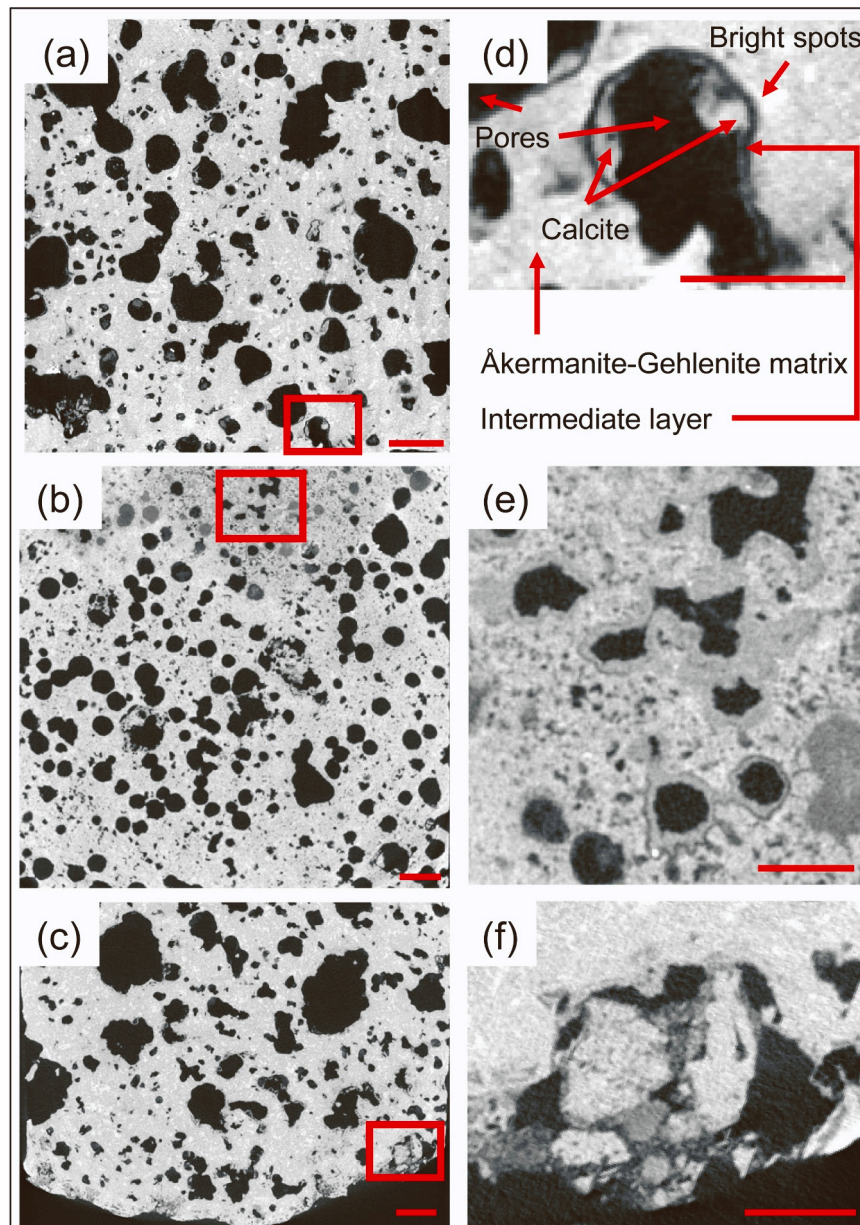|	SiO$_2$/%	Al$_2$O$_3$/%	Fe$_2$O$_3$/%	MgO/%	CaO/%	Na$_2$O/%	K$_2$O/%	TiO$_2$/%	MnO/%
Sample A	34.38	13.66	0.47	7.11	38.78	0.16	0.30	0.81	0.58
Sample B	31.55	13.91	0.17	2.31	42.35	0.39	0.21	0.71	0.53
Sample C	34.25	11.73	0.30	6.37	39.10	0.15	0.49	0.97	1.04
Sample D	32.10	12.19	0.53	7.01	39.35	0.17	0.23	0.59	0.32

Fig. 2. Reconstructed XCT images from samples A(a), B(b) and C(c). Magnified boxed areas in images (a), (b) and (c) are shown on the right column. The scale bars are 1000 μm in images (a, b, c) and 500 μm in images (d, e, f).

X′Celerator detector using the sample spinner stage. Phase identification was carried out with reference to the Crystallographic Open Database (Crystallography Open Database, 2022; Vaitkus et al., 2021) in High-score Plus® software. The thermogravimetric test was performed using SDT Q600 thermogravimetric analyzer (TA Instruments) with a heating rate of 10 °C/min and under argon atmosphere. The uncertainty of the balance used in the TGA instrument is 0.1 μg. XRD and TGA analyses were performed at the School of Chemistry, University of Glasgow. The pulverized offcuts were milled using tungsten carbide ball mill (Retsch,

MM400) and analyzed using Panalytical PW2404 wavelength-dispersive sequential X-ray spectrometer at the XRF Facility, School of Geosciences, University of Edinburgh.

3. Results

Fig. 1(a) displays the TGA curves in which the samples weight loss is expressed as a function of temperature, while Fig. 1(b) displays the derivative thermogravimetric (DTG) curves which show the rate of
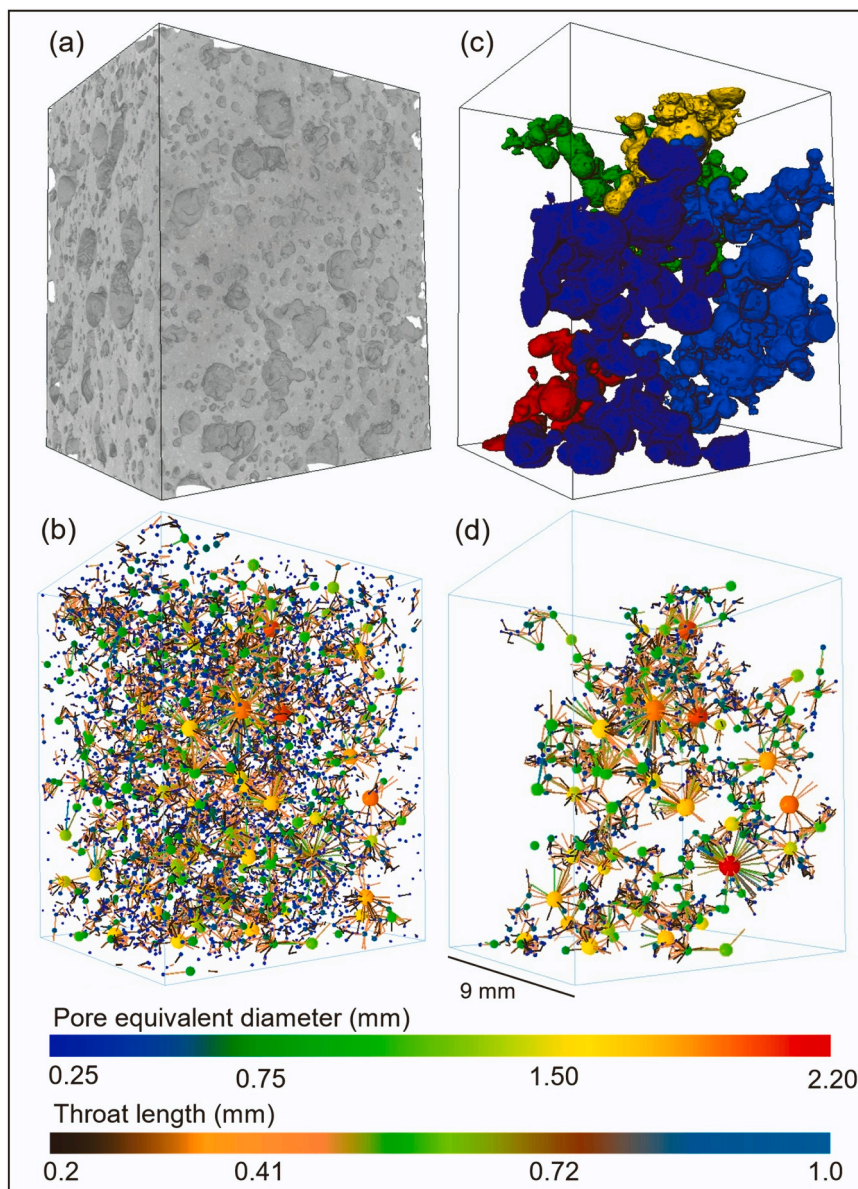
Fig. 3. (a) Visualization of sample A reconstructed from XCT images. (b) Pore network model, showing pores as spheres connected by cylinders. (c) The five largest clusters of connected pore space, where each color represents a distinct cluster. (d) Pore network model of the clusters shown in (c).

weight loss with respect to temperature, and it is used to identify temperatures at which maximum weight loss occurs. Fig. 1(a) and Fig. 1(b) resemble thermal profiles of slag and other alkaline wastes as described in the literature (e.g., Chiang and Pan, 2017). The profiles are characterized by an initial drop in weight due to the removal of free water (50–105 °C), followed by gradual weight loss due to the removal of pore water and crystal water (200–500 °C), and then a drop takes place between 500 and 850 °C due to carbonates decomposition (Chiang and Pan, 2017). Considering that the weight loss between ~600 and ~700 °C is a consequence of calcite decomposition, CO_2 content is calculated by:

$$\%CO_2 = \frac{\Delta m_{CO_2}}{m_{105\,°C}} \tag{4}$$

Where Δm_{CO2} is determined from the TGA/DTG as per the methods reported in Pan et al. (2016) that factor out the weight loss due to non-carbonates mineral decomposition in this temperature range. $m_{105\,°C}$ is the dry weight of the sample measured at T = 105 °C. The CO_2 uptake in the studied samples is between 0.86% and 2.84% by weight,

equivalent to between 8.7 and 29.2 kg CO_2/1000 kg slag on CO_2-free basis. Fig. 1(c) displays the results of the XRD analysis. The studied samples are composed of melilite group minerals, notably åkermanite and gehlenite, as evident from the matching between the samples' diffraction patterns and the reference minerals diffraction patterns. The samples also contain peaks for other minerals such as calcite and pseudowollastonite, although such peaks are less pronounced due to the low abundance of these minerals, causing some of their peaks to be indistinguishable from noise. The XRF analysis (Table 1) shows that the samples are predominantly composed of SiO_2 and CaO, with low Fe_2O_3 content, similar to blast furnace slag compositions reported elsewhere (Chiang and Pan, 2017).

The XCT scans were used to visualize and characterize the internal microstructure of the studied samples. As shown in Fig. 2, the reconstructed data show the pore space in black, while the other components of slag are displayed at higher grey-level values depending on their compositions and attenuation coefficients, and occasionally bright spots appear. These spots represent iron or other metals that were incorporated in the slag during the ironmaking process. Based on the
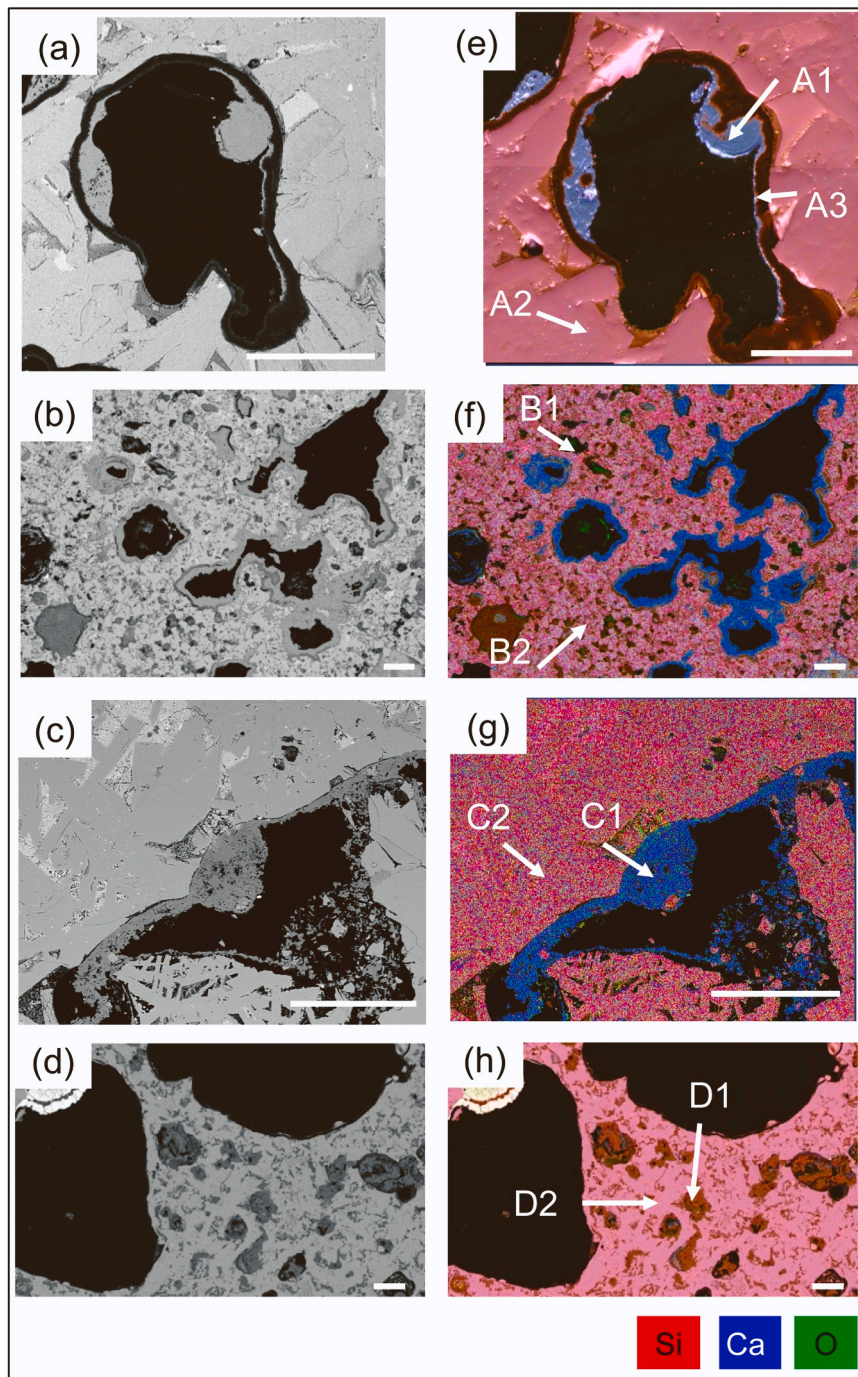
Fig. 4. (a), (b), (c) and (d) are BSE images of the respective studied samples (A, B, C, D) and (e), (f), (g) and (h) are false-color EDS elemental maps. Spectra from annotated areas are displayed in supplementary Figs. S7 and S8. In the EDS maps, black areas represent pores, while pink areas represent Al-, Ca-, Si-, O- containing matrix and the blue area represent Ca- and O- containing precipitates. The scale bars are 250 μm.
Images (b) and (f) were based on data from (Khudhur et al., 2022b).

segmentation results performed on the studied samples, the volume percentages range from 62.1%− 73.8%, 20.1%− 33.4%, 0%− 10.0%, 0.8%− 12.5% for the matrix, pore space, calcite and the miscellaneous phase, respectively, across the analyzed samples (supplementary Figs. S2 and S3). The observed pores, however, form isolated clusters throughout the sample. Pore-network modelling in Fig. 3 (and supplementary Figs. S4, S5 and S6) visualizes the pore space by representing pores as spheres connected by cylinders. The observed pores have variable equivalent diameters, with the average equivalent diameter ranging from 130 μm for sample D to 175 μm for sample C and with

median pore diameters smaller than mean diameters across the studied samples, indicating a right-skewed distribution. Commonly, pores are empty, i.e., the void space is in direct contact with the matrix, as exemplified in Fig. 2. However, Fig. 2 also shows some pores are lined with thin (<50 μm) layers of materials that have different textures and grey-level values when compared to the matrix, and which resemble carbonates layers, also shown in a previous study (Jacquemet et al., 2012). In Figs. 2(a) and 2(b), these layers are bounded by other intermediate layers, separating them from the matrix. Higher resolution BSE images and EDS elemental maps (Fig. 4 and supplementary Figs. S7 and
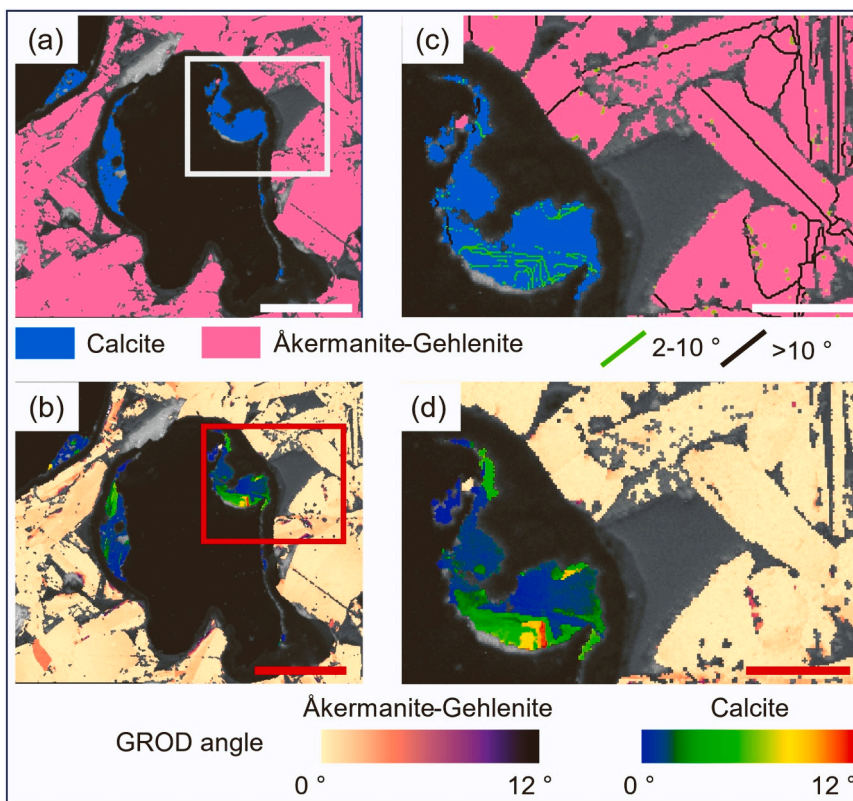
Fig. 5. (a) EBSD phase map and grain boundaries and (b) GROD angle map showing åkermanite-gehlenite and calcite deformation for Sample A, both overlay electron images. Black/grey areas represent pore space and non-indexed pixels. Boxed areas in (a) and (b) are magnified in (c) and (d). The scale bars are 250 in images (a, b) and 100 μm in images (c, d).

S8) demonstrate that the layers closer to the pore space are rich in calcium and oxygen, and the intermediate layers are depleted in Ca, and contain Si and O, while the matrix contains Ca, Si, O, Al and Mg. Across the studied volumes, SEM and EDS results show that some pores are filled with Si-O rich materials (Fig. 4(d) and (h)), possibly indicating the presence of amorphous silica as no other silica-rich minerals were identified from the XRD patterns. Using EBSD, the calcium-rich layer near the pore space is indexed as calcite, (Fig. 5(a) and Fig. 6(a) and supplementary Fig. S9). The EBSD analysis also shows that the matrix is dominated by åkermanite-gehlenite minerals, with a lower presence of pseudowollastonite as depicted in Fig. 6. However, the intermediate Ca-depleted layer between the calcite and åkermanite-gehlenite minerals is not indexed since no pattern can be detected in it, as exemplified from the band contrast image (supplementary Fig. S10). Calcite also precipitates on the external surface of slag, where there is no presence of the intermediate layer that segregated between it and the slag matrix (Fig. 4(g) and supplementary Fig. S9).

The EBSD results were further used to produce grain reference orientation detection (GROD) maps. These maps are generated by determining the average grain orientation, and by determining how the orientation of each pixel within that grain differs from the average grain orientation, and they represent the data in the form of heat maps as depicted in Fig. 5(b) and Fig. 6(b). The provided GROD maps for samples A and B show large misorientation in the calcite crystals and low misorientation in the åkermanite-gehlenite crystals. EBSD analysis further demonstrates that calcite grains contain discontinuous and highly irregular low-angle (<10°) grain boundaries, although for sample C, where calcite precipitated on the external surface of the sample, high-angle grain boundaries prevail, with grains having low deformation, as depicted in supplementary Fig. S9. The pole figures show there is no crystallographic preferred orientation (CPO) for the matrix minerals as well as for calcite (Fig. 7). Additionally, no CPO was found for

åkermanite-gehlenite grains that are at the interface between calcite and the matrix, as depicted in supplementary Fig. S11.

4. Discussion

XRD analysis shows that the studied samples contain åkermanite, gehlenite and calcite. These minerals are commonly found in slag. For example, Grubb and Berggren (2018) reported the presence of åkermanite and gehlenite in blast furnace slag samples collected from Indiana steelworks in the United States. Iacobescu et al. (2013) reported the presence of åkermanite in electric arc furnace slag collected from SOVEL S.A. Industry in Greece, while Chukwuma et al. (2021) reported åkermanite and gehlenite in legacy slag sites across the UK. TGA results reveal typical profiles of TGA tests performed on artificial wastes (Pan et al., 2016), although our analysis did not show any peak in the temperature range between 150 °C and 400 °C. This indicates a lack of Ca(OH)$_2$ in the studied samples, in consistence with the XRD results which show no presence of Ca(OH)$_2$ peaks in the samples diffractograms. This suggests the absence of portlandite in the studied samples or its dissolution prior to sample collection. The calculated values of CO$_2$ uptake in the studied samples (between 8.7 and 29.2 kg CO$_2$/1000 kg slag) are towards the lower end of values reported previously by Wang et al. (2021) and Crouzet et al. (2017), 10–50 g CO$_2$/ kg slag and 63 g CO$_2$/kg slag respectively. While several factors such as slag emplacement conditions can explain this difference, we highlight that this difference can be associated with the different mineralogy between our samples and those of Wang et al. (2021) and Crouzet et al. (2017). XRD analysis illustrates that our studied samples are predominantly composed of melilite group minerals (åkermanite-gehlenite), while those studied by Wang et al. (2021) and Crouzet et al. (2017) were predominantly composed of merwinite and dicalcium silicates. Åkermanite and gehlenite have slower dissolution rates when compared to merwinite and
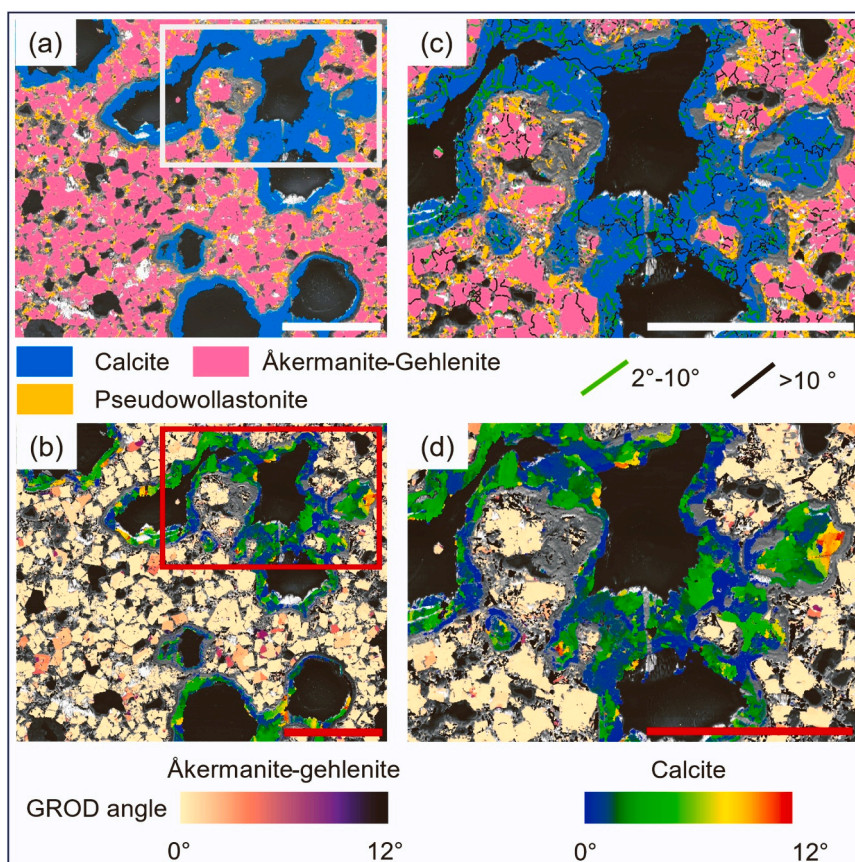
Fig. 6. (a) EBSD phase map and grain boundaries and (b) GROD map showing åkermanite-gehlenite and calcite deformation for Sample B, both overly electron images. Black/grey areas represent pore space and non-indexed pixels. Boxed areas in (a) and (b) are magnified in (c) and (d). The scale bars are 500 μm.

dicalcium silicates (Engström et al., 2013). Through measuring acid consumption at a fixed pH of 10 - which resembles that encountered in slag environment - as a proxy for dissolution rate, Engström et al. (2013) showed that for the same period (~1.5 day), dicalcium silicates, åkermanite, and gehlenite consumed 8 ml, 0.5 ml and ml 0.3 of HNO_3 respectively.

The XCT results were used to gain further insight into the effect of porosity on CO_2 mineralization. Fig. 8(a) shows that the samples are dominated by pores with equivalent diameters < 130 μm, which may alter calcite precipitation rates. This is because ions can still exist in supersaturation states in porous media since precipitation/dissolution reactions display pore-size dependence according to the pore-size controlled solubility concept (Zachara et al., 2016). However, the dependence of rate on pore size is difficult to generalize since it depends on the precipitating material, the substrate and the flow conditions. Several studies have noted that calcite precipitation was favored in macropores (>1 μm) and hindered in nanopores (Stack et al., 2014). In our study, calcite precipitates around pores with various volumes such as ~5×10^{-3} mm^3 and ~1 mm^3, as depicted in Fig. 8. Due to the voxel volume of ~10^3 $μm^3$ that is dictated by the choice of a representative volume size sample, calcite precipitation in nanopores could not be evaluated. We speculate that this is marginal since calcite precipitation in nanopores was previously found to be minimal in the absence of a functionalized self-assembled monolayer that may enhance nucleation density (Stack et al., 2014). Additionally, Fig. 8(a) shows that the studied samples have a right-skewed pore diameter distribution. Steinwinder and Beckingham (2019) explained that such a profile was more prone to pore clogging, with a 5% decrease in porosity resulting in an order of magnitude drop in permeability. Consequently, precipitation of minor amounts of calcite or other materials can result in a large decrease in permeability, thereby reducing the ability of carbonates-rich

solutions to reach the reactive sites within slag lumps.

The microstructure of slag can further demonstrate why the CO_2 uptake is small when compared to CO_2 uptake values found during slag carbonation in reactors which were reported to reach 270 g CO_2/ kg slag in about an hour (Chang et al., 2011). Unlike carbonation in such reactors, which requires prior pulverization of slag to the micron-scale particles, passive CO_2 uptake in slag relies on the exposed surface area of slag and accessible surface areas within slag or the pore surface area. While the studied samples have considerable porosity (23.8%−30.5%), the pore space is made of isolated pores. Consequently, this may result in constricting the flow of water that contains carbonate ions to reactive sites thereby reducing the amount of mineralized CO_2. Previous experimental work showed that calcite precipitation caused pore clogging and was likely to inhibit further delivery of ions to the reactive areas thereby hindering the CO_2 mineralization process (Baek et al., 2019; Noiriel et al., 2012). We also previously showed that calcite precipitation within slag decreased the pores connectivity which can consequently further restrict fluids flow to reactive surface sites (Khudhur et al., 2022b). This problem is further intensified if calcite precipitation occurs at the surface of slag as shown in supplementary Fig. S9, since this precipitation pattern can form a barrier that isolates reactive minerals within slag, analogous to precipitation observed in column experiments where calcite precipitation occurred within the top 2 mm of the studied volume (Noiriel et al., 2012).

Another reason that explains low CO_2 uptake is the formation of Si-O rich phases in slag as demonstrated in Fig. 4(d) and (h). Such phases can precipitate from water that percolates the slag heap, and can consequently reduce the permeability of the medium in which they form (Malate and O'Sullivan, 1992). Benhelal et al. (2020) reported that during the mineral carbonation of lizardite, Si leached out and polymerized in the solution, and then precipitated as amorphous silica, and
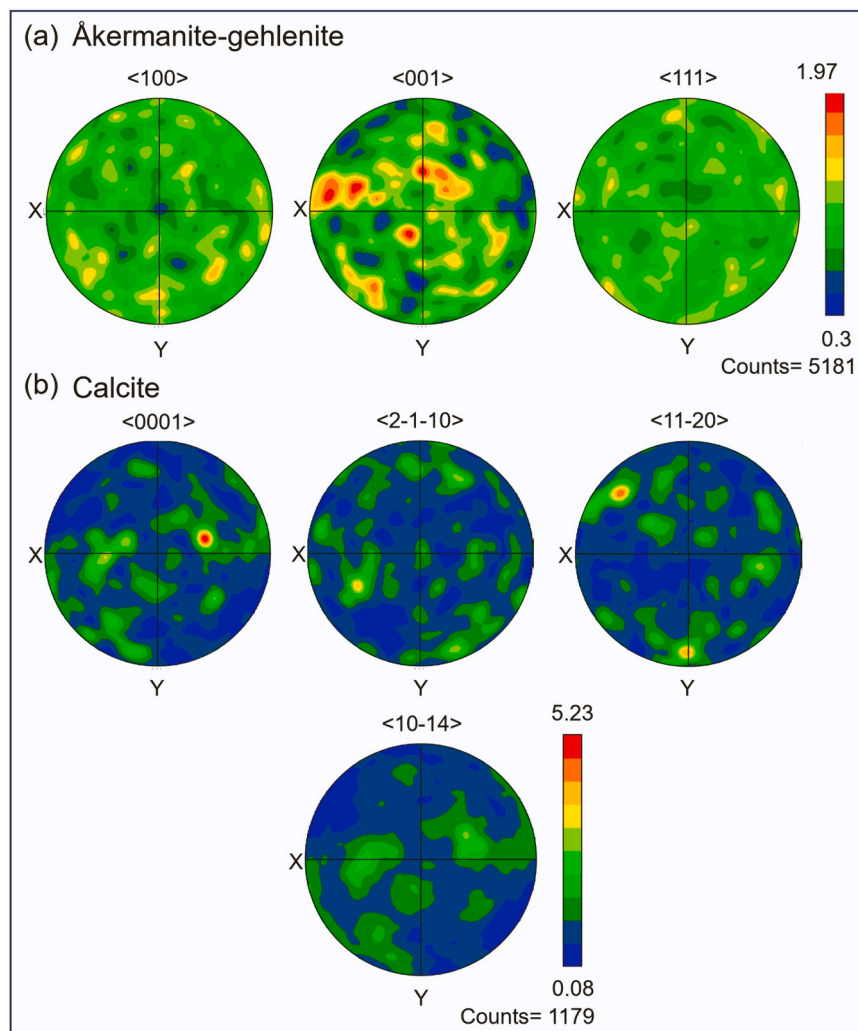
Fig. 7. (a) Åkermanite-gehlenite pole figures and (b) calcite pole figures for sample B. Color bars are in multiples of uniform density (MUD) unit.

they demonstrated that this could hinder CO_2 uptake through the following ways: firstly, amorphous silica can cover reactive sites thereby preventing them from participating in further reactions. Secondly, this layer can adsorb cations and prevent them from reacting with CO_3^{2-} to precipitate carbonates. Another Si-O rich region observed in this study is the Ca-depleted intermediate layer between the precipitated calcite and åkermanite-gehlenite phases. The possibility of forming such a layer has been discussed in the literature, mostly when mineralization was studied during the carbonation of pulverized samples. Ragipani et al. (2020) studied slag carbonation using the pH-swing method, and they concluded that no such layer formed during the mineral carbonation of slag. In this study, as well as in the previous research (Lekakh et al., 2008; MacDonald et al., 2023), the development of such layers is evident. We attribute this difference to the fact that in the study of Ragipani et al. (2020), the used slag contained orthosilicates, which have similar reactivity to that of metal oxides and dissolve uniformly, while in our research the slag is dominated by sorosilicates (åkermanite-gehlenite) which exhibit slow dissolution that is likely to result in the formation of a Si-O rich rim observed when calcite precipitates, therefore acting as a passivating layer and hindering the CO_2 mineralization process (Engström et al., 2013; Ragipani et al., 2020; Terry, 1983). As slag is a heterogenous mixture with compositions that depend on the used ore composition and processing pathway, it contains several impurities that inhibit carbonates precipitation. For example, previous studies showed that different cations and ligands inhibited calcite precipitation due to complexation and adsorption effects (Morse et al.,

2007; Power et al., 2013). Experimental observations during the evaluation of chrysotile mine residue for CO_2 mineralization also documented that the presence of iron inhibited this process due to the formation of iron hydroxide, which formed an impermeable layer to water and prevented further minerals dissolution and cation supply, thereby reducing the overall CO_2 uptake (Assima et al., 2013, 2012). However, no such layers are observed in our studied samples.

The microstructural analysis by EBSD provides further details about the nature of CO_2 mineralization. Calcite exhibits short, low-angle grain boundaries with sub-grains that are highly irregular in shape, and its GROD maps show more pronounced misorientation microstructure within the grains when compared to those of åkermanite-gehlenite. Spruzeniece et al. (2017) showed that such microstructures can form in the product phases of dissolution-precipitation reactions, even in the absence of deformation. The pole figures in Fig. 7 indicate that there are no crystallographic correlation between the reactive åkermanite-gehlenite substrate and the precipitated calcite grains, suggesting non-topotactic growth of calcite. Peuble et al. (2015) observed similar behavior while studying CO_2 mineralization in olivine, where carbonate precipitation was heterogenous throughout the sample and was controlled by the fluid flow pattern. Precipitation occurred in secondary and low flow rate zones that allow for local supersaturation and precipitation, suggesting that controlling the watering hydrodynamics can enhance the CO_2 mineralization process. While it is common for carbonates such as calcite and magnesite to grow in the {10−14} direction (e.g., (Mayorga et al., 2018)), this is not observed in the current study.
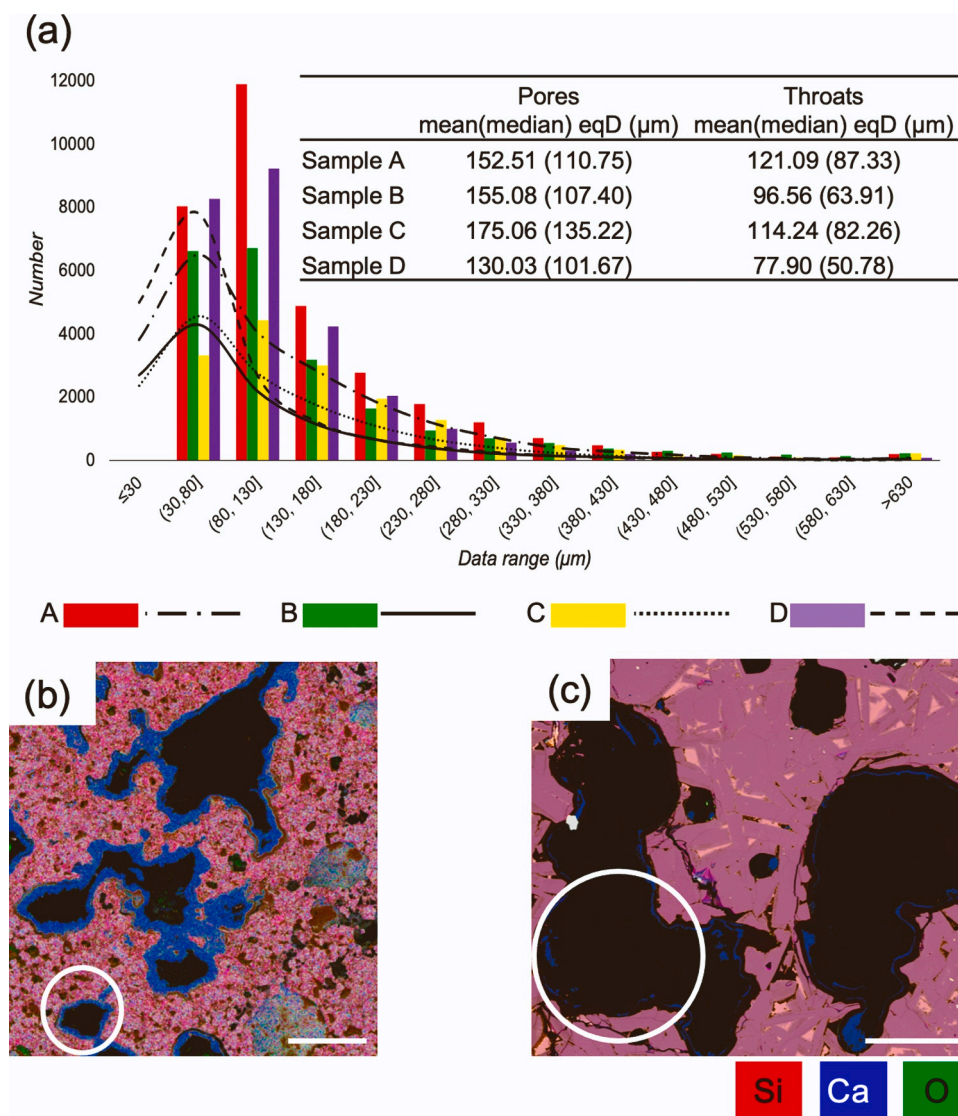
Fig. 8. (a) Pore equivalent diameters (bars) and throat equivalent diameters (dashed lines) of the studied samples. (b), (c) EDS maps that demonstrate calcite precipitation in a small pore (circled) in (b) and in large pores (c). Scale bars are 500 μm.
Image (b) is based on data from Khudhur et al. (2022b)).

We attribute this to rapid precipitation process that occurred because of supersaturations in the pore space.

5. Conclusions

Previous research that was based on slag chemistry calculated CO_2 uptake potential of ~ 400 g CO_2/ kg slag (Renforth, 2019). There are, however, several factors that may reduce CO_2 uptake through passive mineralization in slag. Our observations from the former Ravenscraig site in Scotland show that achievable CO_2 uptake in the collected samples was 9–29 g CO_2/kg slag after ~30 years of exposure to the atmosphere. This work concludes that mineralogical and microstructural factors should be considered for the accurate forecast of CO_2 uptake through passive mineralization in slag. The samples that we collected from Ravenscraig legacy site in Scotland are pluri-centimetric, with porous media that can form isolated pore clusters, resulting in a lack of access of HCO_3 and CO_3^{-2}-rich fluid to reactive surface area within slag. Another factor that can reduce the CO_2 uptake in slag is the observed Si-O components that form during the passive mineralization of slag due to interaction with water. Formation of these components, in addition to calcite formation as a consequence of mineralization, can result in

inhabiting further CO_2 mineralization due to the surface passivation effect. Additionally, the studied samples contain melilite group minerals such as åkermanite and gehlenite. These minerals have been documented in slags produced worldwide, however, their dissolution rates are slow when compared with other slag-forming minerals such as larnite. Size-reduction of slag increases the available surface area which can enhance the CO_2 mineralization reaction but can also enhance the mobility of impurities that can have a polluting effect. While passive CO_2 mineralization in slag is a promising carbon capture technique, it requires further kinetic, economic and lifecycle assessment prior to its deployment as a large-scale CO_2 uptake method.

Declaration of Competing Interest

The authors declare that they have no known competing financial interests or personal relationships that could have appeared to influence the work reported in this paper.

Data Availability

Data will be made available on request.

Associated content

Supplementary material to this article includes XCT and SEM equipment settings, further image processing details and further EDS and EBSD results. The data used in this manuscript are available upon request from the corresponding author.

Appendix A. Supporting information

Supplementary data associated with this article can be found in the online version at doi:10.1016/j.micron.2023.103532.

References

Assima, G.P., Larachi, F., Beaudoin, G., Molson, J., 2012. CO_2 sequestration in chrysotile mining residues—implication of watering and passivation under environmental conditions. Ind. Eng. Chem. Res. 51, 8726–8734. https://doi.org/10.1021/IE202693Q.

Assima, G.P., Larachi, F., Beaudoin, G., Molson, J., 2013. Dynamics of carbon dioxide uptake in chrysotile mining residues – Effect of mineralogy and liquid saturation. Int. J. Greenh. Gas. Control 12, 124–135. https://doi.org/10.1016/J.IJGGC.2012.10.001.

Baek, S.H., Hong, J.W., Kim, K.Y., Yeom, S., Kwon, T.H., 2019. X-Ray computed microtomography imaging of abiotic carbonate precipitation in porous media from a supersaturated solution: insights into effect of CO_2 mineral trapping on permeability. Water Resour. Res. 55, 3835–3855. https://doi.org/10.1029/2018WR023578.

Béarat, H., McKelvy, M.J., Chizmeshya, A.V.G., Gormley, D., Nunez, R., Carpenter, R.W., Squires, K., Wolf, G.H., 2006. Carbon sequestration via aqueous olivine mineral carbonation: role of passivating layer formation. Environ. Sci. Technol. 40, 4802–4808. https://doi.org/10.1021/es0523340.

Benhelal, E., Oliver, T.K., Farhang, F., Hook, J.M., Rayson, M.S., Brent, G.F., Stockenhuber, M., Kennedy, E.M., 2020. Structure of silica polymers and reaction mechanism for formation of silica-rich precipitated phases in direct aqueous carbon mineralization. Ind. Eng. Chem. Res. 59, 6828–6839. https://doi.org/10.1021/acs.iecr.9b04379.

Boone, M.A., Nielsen, P., De Kock, T., Boone, M.N., Quaghebeur, M., Cnudde, V., 2014. Monitoring of stainless-steel slag carbonation using X-ray computed microtomography. Environ. Sci. Technol. 48, 674–680. https://doi.org/10.1021/es402767q.

Chang, E.E., Chen, C.H., Chen, Y.H., Pan, S.Y., Chiang, P.C., 2011. Performance evaluation for carbonation of steel-making slags in a slurry reactor. J. Hazard. Mater. 186, 558–564. https://doi.org/10.1016/j.jhazmat.2010.11.038.

Chiang, P.C., Pan, S.Y., 2017. Carbon dioxide mineralization and utilization. Carbon Dioxide Miner. Util. https://doi.org/10.1007/978-981-10-3268-4.

Chukwuma, J.S., Pullin, H., Renforth, P., 2021. Assessing the carbon capture capacity of South Wales' legacy iron and steel slag. Miner. Eng. 173, 107232 https://doi.org/10.1016/J.MINENG.2021.107232.

Crouzet, C., Brunet, F., Montes-Hernandez, G., Recham, N., Findling, N., Ferrasse, J.H., Goffé, B., 2017. Hydrothermal valorization of steel slags-Part I: Coupled H_2 production and CO_2 mineral sequestration. Front. Energy Res. 5, 1–12. https://doi.org/10.3389/fenrg.2017.00029.

Crystallography Open Database [WWW Document], 2022. URL http://www.crystallography.net/cod/ (Accessed 12.6.22).

Engström, F., Adolfsson, D., Samuelsson, C., Sandström, Å., Björkman, B., 2013. A study of the solubility of pure slag minerals. Miner. Eng. 41, 46–52. https://doi.org/10.1016/J.MINENG.2012.10.004.

Gomes, H.I., Mayes, W.M., Rogerson, M., Stewart, D.I., Burked, I.T., 2016. Alkaline residues and the environment: a review of impacts, management practices and opportunities. J. Clean. Prod. https://doi.org/10.1016/j.jclepro.2015.09.111.

Gomes, H.I., Mayes, W.M., Baxter, H.A., Jarvis, A.P., Burke, I.T., Stewart, D.I., Rogerson, M., 2018. Options for managing alkaline steel slag leachate: a life cycle assessment. J. Clean. Prod. 202, 401–412. https://doi.org/10.1016/J.JCLEPRO.2018.08.163.

Gostick, J., Aghighi, M., Hinebaugh, J., Tranter, T., Hoeh, M.A., Day, H., Spellacy, B., Sharqawy, M.H., Bazylak, A., Burns, A., Lehnert, W., Putz, A., 2016. OpenPNM: a pore network modeling package. Comput. Sci. Eng. 18, 60–74. https://doi.org/10.1109/MCSE.2016.49.

Griffin, S., Udry, A., Daly, L., Forman, L.V., Lee, M.R., Cohen, B.E., 2023. Investigating the igneous petrogenesis of Martian volcanic rocks using augite quantitative textural analysis of the Yamato nakhlites. Meteorit. Planet. Sci. 58, 63–84. https://doi.org/10.1111/MAPS.13934.

Grubb, D.G., Berggren, D.R.V., 2018. Air-cooled blast furnace slag. I: Characterization and leaching context. J. Hazard., Toxic., Radioact. Waste 22, 04018030. https://doi.org/10.1061/(ASCE)HZ.2153-5515.0000411.

Gunning, P.J., Hills, C.D., Carey, P.J., 2010. Accelerated carbonation treatment of industrial wastes. Waste Manag 30, 1081–1090. https://doi.org/10.1016/j.wasman.2010.01.005.

Huijgen, W.J.J., Witkamp, G.J., Comans, R.N.J., 2005. Mineral CO_2 sequestration by steel slag carbonation. Environ. Sci. Technol. 39, 9676–9682. https://doi.org/10.1021/es050795f.

Huntzinger, D.N., Gierke, J.S., Kawatra, S.K., Eisele, T.C., Sutter, L.L., 2009. Carbon dioxide sequestration in cement kiln dust through mineral carbonation. Environ. Sci. Technol. 43, 1986–1992. https://doi.org/10.1021/es802910z.

Iacobescu, R.I., Pontikes, Y., Koumpouri, D., Angelopoulos, G.N., 2013. Synthesis, characterization and properties of calcium ferroaluminate belite cements produced with electric arc furnace steel slag as raw material. Cem. Concr. Compos. 44, 1–8. https://doi.org/10.1016/J.CEMCONCOMP.2013.08.002.

Ioris, A.A.R., 2014. The urban political ecology of post-industrial scottish towns: examining greengairs and ravenscraig. Urban Stud. 51, 1576–1592. https://doi.org/10.1177/0042098013497408.

Jacquemet, N., Pironon, J., Lagneau, V., Saint-Marc, J., 2012. Armouring of well cement in H_2S–CO_2 saturated brine by calcite coating – Experiments and numerical modelling. Appl. Geochem. 27, 782–795. https://doi.org/10.1016/J.APGEOCHEM.2011.12.004.

Khudhur, F.W., MacDonald, J.M., Macente, A., Daly, L., 2022a. The utilization of alkaline wastes in passive carbon capture and sequestration: promises, challenges and environmental aspects. Sci. Total Environ. 823, 153553 https://doi.org/10.1016/J.SCITOTENV.2022.153553.

Khudhur, F.W.K., Macente, A., MacDonald, J.M., Daly, L., 2022b. Image-based analysis of weathered slag for calculation of transport properties and passive carbon capture. Microsc. Micro 28, 1514–1525. https://doi.org/10.1017/S1431927622000915.

Lackner, K.S., Wendt, C.H., Butt, D.P., Joyce, E.L., Sharp, D.H., 1995. Carbon dioxide disposal in carbonate minerals. Energy 20, 1153–1170. https://doi.org/10.1016/0360-5442(95)00071-N.

Land Use Consultant, 2008. Ravenscraig Green Network Strategy [WWW Document]. URL ⟨https://www.gcvgreennetwork.gov.uk/publications/277-ravenscraig-green-network-strategy/file⟩ (accessed 8.10.23).

Lekakh, S.N., Rawlins, C.H., Robertson, D.G.C., Richards, V.L., Peaslee, K.D., 2008. Kinetics of aqueous leaching and carbonization of steelmaking slag. Metall. Mater. Trans. B Process. Metall. Mater. Process. Sci. 39, 125–134. https://doi.org/10.1007/s11663-007-9112-8.

MacDonald, J.M., Khudhur, F.W.K., Carter, R., Plomer, B., Wilson, C., Slaymark, C., 2023. The mechanisms and microstructures of passive atmospheric CO_2 mineralisation with slag at ambient conditions. Appl. Geochem. 152, 105649 https://doi.org/10.1016/J.APGEOCHEM.2023.105649.

Malate, R.C.M., O'Sullivan, M.J., 1992. Mathematical modelling of silica deposition in a porous medium. Geothermics 21, 377–400. https://doi.org/10.1016/0375-6505(92)90088-Q.

Mariano, R.G., McKelvey, K., White, H.S., Kanan, M.W., 2017. Selective increase in CO_2 electroreduction activity at grain-boundary surface terminations (80-). Science 358, 1187–1192. https://doi.org/10.1126/science.aao3691.

Mayes, W.M., Riley, A.L., Gomes, H.I., Brabham, P., Hamlyn, J., Pullin, H., Renforth, P., 2018. Atmospheric CO_2 sequestration in iron and steel slag: consett, County Durham, United Kingdom. Environ. Sci. Technol. 52, 7892–7900. https://doi.org/10.1021/acs.est.8b01883.

Mayorga, I.C., Astilleros, J.M., Fernández-Díaz, L., Morales, J., Prieto, M., Roncal-Herrero, T., Benning, L.G., 2018. Epitactic overgrowths of calcite ($CaCO_3$) on anhydrite ($CaSO_4$) cleavage surfaces. Cryst. Growth Des. 18, 1666–1675. https://doi.org/10.1021/acs.cgd.7b01610.

Met Office, 2016. Western Scotland: climate [WWW Document]. URL ⟨https://www.metoffice.gov.uk/binaries/content/assets/metofficegovuk/pdf/weather/learn-about/uk-past-events/regional-climates/western-scotland_-climate—met-office.pdf⟩ (Accessed 8.16.23).

Morse, J.W., Arvidson, R.S., Lüttge, A., 2007. Calcium carbonate formation and dissolution. Chem. Rev. 107, 342–381. https://doi.org/10.1021/cr050358j.

Noiriel, C., Steefel, C.I., Yang, L., Ajo-Franklin, J., 2012. Upscaling calcium carbonate precipitation rates from pore to continuum scale. Chem. Geol. 318–319, 60–74. https://doi.org/10.1016/J.CHEMGEO.2012.05.014.

Pan, S.Y., Chang, E.E., Kim, H., Chen, Y.H., Chiang, P.C., 2016. Validating carbonation parameters of alkaline solid wastes via integrated thermal analyses: principles and applications. J. Hazard. Mater. 307, 253–262. https://doi.org/10.1016/J.JHAZMAT.2015.12.065.

Peuble, S., Andreani, M., Godard, M., Gouze, P., Barou, F., Van De Moortele, B., Mainprice, D., Reynard, B., 2015. Carbonate mineralization in percolated olivine aggregates: Linking effects of crystallographic orientation and fluid flow. Am. Mineral. 100, 474–482. https://doi.org/10.2138/am-2015-4913.

Power, I.M., Harrison, A.L., Dipple, G.M., Wilson, S.A., Kelemen, P.B., Hitch, M., Southam, G., 2013. Carbon mineralization: from natural analogues to engineered systems. Rev. Mineral. Geochem. 77, 305–360. https://doi.org/10.2138/rmg.2013.77.9.

Pullin, H., Bray, A.W., Burke, I.T., Muir, D.D., Sapsford, D.J., Mayes, W.M., Renforth, P., 2019. Atmospheric carbon capture performance of legacy iron and steel waste. Environ. Sci. Technol. 53, 9502–9511. https://doi.org/10.1021/acs.est.9b01265.

Ragipani, R., Bhattacharya, S., Akkihebbal, S.K., 2020. Understanding dissolution characteristics of steel slag for resource recovery. Waste Manag 117, 179–187. https://doi.org/10.1016/J.WASMAN.2020.08.008.

Renforth, P., 2019. The negative emission potential of alkaline materials. Nat. Commun. 10, 1401. https://doi.org/10.1038/s41467-019-09475-5.

Renforth, P., Washbourne, C.-L., Taylder, J., Manning, D.A.C., 2011. Silicate production and availability for mineral carbonation. Environ. Sci. Technol. 45, 2035–2041. https://doi.org/10.1021/es103241w.

Renforth, P., von Strandmann, Pogge, Henderson, G.M, P.A.E., 2015. The dissolution of olivine added to soil: Implications for enhanced weathering. Appl. Geochem. 61, 109–118. https://doi.org/10.1016/j.apgeochem.2015.05.016.

Riley, A.L., MacDonald, J.M., Burke, I.T., Renforth, P., Jarvis, A.P., Hudson-Edwards, K. A., McKie, J., Mayes, W.M., 2020. Legacy iron and steel wastes in the UK: Extent, resource potential, and management futures. J. Geochem. Explor 219, 106630. https://doi.org/10.1016/j.gexplo.2020.106630.

Spruzeniece, L., Piazolo, S., Maynard-Casely, H.E., 2017. Deformation-resembling microstructure created by fluid-mediated dissolution-precipitation reactions. Nat. Commun. 8, 1–9. https://doi.org/10.1038/ncomms14032.

Stack, A.G., Fernandez-Martinez, A., Allard, L.F., Bañuelos, J.L., Rother, G., Anovitz, L. M., Cole, D.R., Waychunas, G.A., 2014. Pore-size-dependent calcium carbonate precipitation controlled by surface chemistry. Environ. Sci. Technol. 48, 6177–6183. https://doi.org/10.1021/es405574a.

Steinwinder, J., Beckingham, L.E., 2019. Role of pore and pore-throat distributions in controlling permeability in heterogeneous mineral dissolution and precipitation

scenarios. Water Resour. Res. 55, 5502–5517. https://doi.org/10.1029/2019WR024793.

Stewart, D., 2008. Fighting for survival: the 1980s campaign to save ravenscraig steelworks. J. Scott. Hist. Stud. 25, 40–57. https://doi.org/10.3366/JSHS.2005.25.1.40.

Sun, H., Wang, J., Liu, X., Shen, B., Parlett, C.M.A., Adwek, G.O., John Anthony, E., Williams, P.T., Wu, C., 2019. Fundamental studies of carbon capture using CaO-based materials. J. Mater. Chem. A 7, 9977–9987. https://doi.org/10.1039/C8TA10472G.

Terry, B., 1983. The acid decomposition of silicate minerals part I. Reactivities and modes of dissolution of silicates. Hydrometallurgy 10, 135–150. https://doi.org/10.1016/0304-386X(83)90002-6.

Vaitkus, A., Merkys, A., Gražulis, S., 2021. Validation of the crystallography open database using the crystallographic information framework. J. Appl. Crystallogr 54, 661–672. https://doi.org/10.1107/S1600576720016532.

Wang, Y., Zeng, Y., Li, J., Zhang, Y., Wang, W., 2021. Properties of ten-year-aged argon oxygen decarburization stainless steel slag. J. Iron Steel Res. Int. 28, 1233–1242. https://doi.org/10.1007/s42243-021-00635-w.

World Steel Association, 2017. Steel Industry co-products [WWW Document]. URL ⟨https://www.worldsteel.org/publications/position-papers/co-product-position-paper.html⟩ (Accessed 10.14.19).

Zachara, J., Brantley, S., Chorover, J., Ewing, R., Kerisit, S., Liu, C., Perfect, E., Rother, G., Stack, A.G., 2016. Internal domains of natural porous media revealed: critical locations for transport, storage, and chemical reaction. Environ. Sci. Technol. 50, 2811–2829. https://doi.org/10.1021/acs.est.5b05015.

Zagorac, D., Müller, H., Ruehl, S., Zagorac, J., Rehme, S., 2019. Recent developments in the inorganic crystal structure database: theoretical crystal structure data and related features. J. Appl. Crystallogr 52, 918–925. https://doi.org/10.1107/S160057671900997X.